# Cross sections and analyzing powers $A_y$ in the breakup reaction $^2\mathrm{H}(\vec{p},pp)n$ at 65 MeV: Star configurations

J. Zejma,* M. Allet, K. Bodek,* J. Lang, R. Müller, S. Navert, O. Naviliat-Cuncic, J. Sromicki, and E. Stephan†
*Institut für Teilchenphysik, Eidgenössische Technische Hochschule, Zürich, Switzerland*

L. Jarczyk, St. Kistryn, J. Smyrski, and A. Strzałkowski
*Institute of Physics, Jagellonian University, Cracow, Poland*

W. Glöckle, J. Golak,* D. Hüber, and H. Witała*
*Institut für Theoretische Physik II, Ruhr-Universität, Bochum, Germany*

P. A. Schmelzbach
*Paul-Scherrer-Institut, Villigen, Switzerland*
(Received 3 June 1996)

Cross-section and vector-analyzing-power data for three star configurations of the $^2\mathrm{H}(\vec{p},pp)n$ breakup reaction at $E_p^{\mathrm{lab}}=65$ MeV were measured in a kinematically complete experiment. They are compared to rigorous Faddeev calculations involving five realistic charge-dependent nucleon-nucleon potentials: Argonne $v_{18}$, CD Bonn, Nijmegen 93, Nijmegen I, and Nijmegen II. A general satisfactory agreement between theory and experiment has been found. However, there exist also a few minor discrepancies in cross sections in some regions of phase space. The experimental data are compared also to the calculations including the $(\pi\text{-}\pi)$ Tucson-Melbourne three-body force. Their effects are either negligible or increase the disagreement with the experiment. [S0556-2813(97)01601-4]

PACS number(s): 21.45.+v, 24.10.−i, 24.70.+s, 25.40.−h

## I. INTRODUCTION

Understanding the nucleon-nucleon ($NN$) interaction is one of the most fundamental goals of nuclear physics. Several meson-exchange models provide realistic two-nucleon ($2N$) potentials which describe satisfactorily the bulk of the $2N$ data. However, the $2N$ system cannot determine uniquely the $NN$ interaction, and it is therefore mandatory to study the three- or many-nucleon systems or the $NN$ bremsstrahlung. Of special importance is the three-nucleon ($3N$) system. Here one can study the bound states of $^3$H and $^3$He nuclei or probe the $NN$ interaction in the elastic nucleon-deuteron ($Nd$) scattering or in the $Nd$-breakup process. The $Nd$-breakup process, where three free nucleons appear in the final state, may deliver very rich physical information since nucleon momenta are not integrated over the deuteron wave function. In particular, the possibility of choosing selected kinematical configurations for the outgoing nucleons allows a concentration on specific properties of the $NN$ interaction. Moreover, for the $3N$ system the observables can be calculated in an exact way by using the Faddeev formalism with both $2N$ and $3N$ forces [1,2]. Thus a comparison of the theoretical predictions with the experimental data provides a direct test of the physical assumptions not obscured by computational approximations. An attempt is made to answer the following questions: Do calculations with two-body realistic potentials describe $3N$ observables? Is it necessary to include genuine $3N$ forces in addition to $2N$ ones? Is the influence of the long-range Coulomb force important?

The above questions can be answered only when a copious set of accurate experimental data is available. In contrast to the elastic $Nd$ scattering, where precise experiments are quite abundant ([3,4] and references therein), the existing database is still insufficient for the breakup reaction. The majority of the breakup experiments was performed at small energies of the incident particles (10–15 MeV); see, e.g., Refs. [5–9] for the $nd$ and [5,10,11] for the $pd$ reactions. In addition, the results of these experiments are not unambiguous. Particularly, serious discrepancies are observed in measurements of the symmetric space star (SSS) configuration [7–9,11]. It is supposed that the observed differences in the cross sections for the $nd$ and $pd$ reactions are, at least partially, caused by the Coulomb force. Therefore, several investigations [3,12–15] were performed at a higher energy (about 65 MeV), where the Coulomb-force effects ought to be small and the relativistic effects ought to be still not significant. Besides the $^2\mathrm{H}(\vec{p},ppn)$, the $^1\mathrm{H}(\vec{d},ppn)$ breakup reaction was also investigated [16], where both vector- and tensor-analyzing powers were measured at a deuteron kinetic energy of 52.1 MeV.

The aim of the present work was to extend the experimental database required to answer the above questions. To this end, some kinematically complete measurements of the differential cross sections and the vector-analyzing powers in the $^2\mathrm{H}(\vec{p},pp)n$ reaction at the incident proton energy of 65

*On leave from Institute of Physics, Jagellonian University, Cracow, Poland.

†On leave from Institute of Physics, University of Silesia, Katowice, Poland.

 

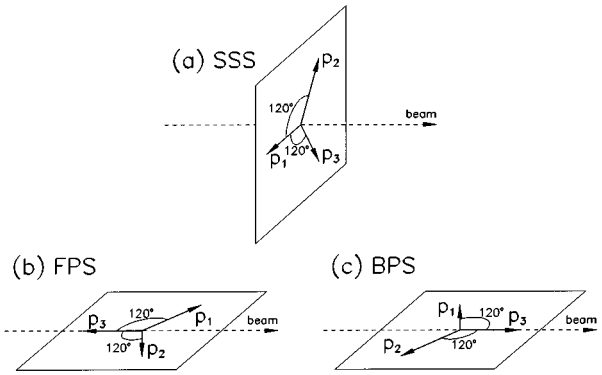


FIG. 1. Momenta of particles in the final state of the $pd$ breakup reaction. The definition of the three kinematical star configurations are presented in the center-of-mass system. The full definitions are given in the text.

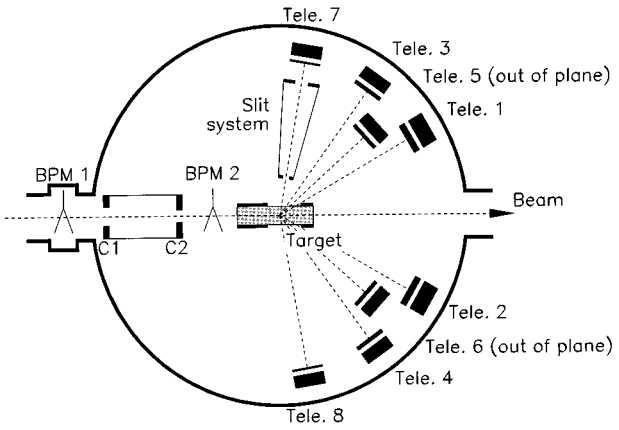


FIG. 2. Schematic view of the chamber interior. All shielding materials are omitted. One detector slit system only is shown as an example. The abbreviations used are explained in the text.

MeV have been performed. While our previous experiments focused on collinearity [3] and quasifree scattering (QFS) [14] configurations, the present one has been devoted mainly to the symmetric space star configuration. The kinematic conditions of the SSS configurations are as follows: The center-of-mass momentum vectors of the particles in the final state $\vec{p}_1$, $\vec{p}_2$, and $\vec{p}_3$ lie in the plane perpendicular to the beam direction [see Fig. 1(a)], and the absolute values of these momenta are equal. This configuration as well as earlier investigated collinearity configurations is supposed to be sensitive to $3N$-force effects, which was suggested by simple model calculations including the $3N$ force at an energy of about 10 MeV [17]. Additionally, the symmetric forward plane star (FPS) and symmetric backward plane star (BPS) configurations have been measured. The difference between these plane stars and the space star is that the momentum vectors of the incident proton and final state nucleons lie in the same plane. For the FPS configuration, the particle not registered (neutron) is emitted opposite to the beam direction, and both registered particles (protons) are sent into the forward hemisphere [Fig. 1(b)]. In the BPS configuration, the momentum vector of the particle not registered is parallel to the beam direction [Fig. 1(c)].

The terms FPS, BPS, and SSS are used throughout the text to define the detector settings which lead to the specific breakup configurations described above. These settings also include breakup configurations where the energy is distributed differently from those specific ones.

The next section presents the description of the experimental equipment and the data analysis. The experimental uncertainties are also discussed there. The theoretical calculations are briefly sketched in Sec. III. The final results of the experiment and their comparison to the theoretical predictions (with and without the three-body force included in the calculations) are presented in Sec. IV. In Sec. V a short summary and outlook are given.

## II. EXPERIMENT

### A. Experimental setup

The experiment was performed at the Philips Cyclotron of the Paul Scherrer Institute in Villigen, Switzerland. A transversally polarized proton beam (polarization of about 80%) with an energy of 65 MeV and an intensity of about 250 nA was used throughout the experiment. To reduce systematic errors the proton-beam polarization was flipped between states ''up'' and ''down'' every second by switching the radio-frequency transition in the ion source. The beam was first focused on the polarimeter target, afterwards focused again on the deuterium gas target, and finally stopped in the Faraday cup.

The beam polarization was continuously monitored by observing the rate asymmetry for protons elastically scattered from a 200-$\mu$g/cm$^2$-thick, self-supporting natural carbon foil. Energy loss and angular straggling in the foil were small (2 keV and 0.1 mrad, respectively) so that the quality of the transmitted beam was not affected. Protons from the $\vec{p}+{}^{12}$C scattering were detected in two NaI scintillation detectors, placed symmetrically on both sides of the beam at $\vartheta^{\rm lab}=45.8°$, where the analyzing power reaches a maximum of $0.9985\pm0.0015$ [18].

A schematic view of the arrangement inside the scattering chamber [19] is shown in Fig. 2. The target container was a $224\times30\times50$ mm$^3$ stainless-steel block, with a cylindrical channel of 16 mm diameter, and was placed in the center of the chamber. It was filled with standard, high-purity (99.7%) deuterium gas. The target cell was equipped with three windows. Two of them, the entrance and exit windows of the proton beam, were made of 3-$\mu$m-thick Havar foil. The reaction products left the target through a 12-$\mu$m-thick Kapton window. The shape of the opening allowed the particles to reach detectors placed on both sides and above the target. The target was cooled down to liquid nitrogen temperature. In order to prevent leakage of atmospheric gases and other impurities into the gas target, the gas-handling system kept the gas pressure slightly higher than the atmospheric one. The two beam-profile monitors (BPM1 and BPM2) were mounted to control the beam position on the target. They were separated by two collimators with circular apertures, C1 and C2 (20 and 7 mm diameter, respectively), insulated from the ground.

Charged particles leaving the target were detected by eight $\Delta E$-$E$ telescopes built from plastic scintillator NE102A. The use of the $\Delta E$-$E$ telescopes allowed us to

separate protons from deuterons and to eliminate a large part of the gamma background. The thicknesses of the $\Delta E$ scintillators (0.2, 0.4, and 2.0 mm) were optimized for the required energy range, whereas the thicknesses of the $E$ scintillators (25 and 35 mm) were adjusted to stop protons elastically scattered on deuterons. The scintillators were coupled to Philips XP2012 photomultipliers except for the 0.2-mm-thick scintillators, which were read out by two Philips XP1911 photomultiplier tubes each. The energy resolution of the detectors was 0.9–1.3 MeV full width at half maximum (FWHM) (including kinematical broadening due to the finite angular acceptance). In front of telescopes 1 and 2, $(3.900 \pm 0.005)$-mm-thick aluminum absorbers were installed on remote-controlled pneumatic pistons. They were used in the energy calibration measurements. All thick detectors were equipped with light-emitting diodes, whose light flashes were used to control gain shifts during the energy calibration measurements.

The slit system used (see Fig. 2 and corresponding text in Ref. [3]) defined the solid angle and the range of accepted angles for each telescope. Since the breakup cross section was normalized with the help of $pd$ elastic-scattering data, not only coincidences (measured by the telescope pairs), but also single events were collected, simultaneously. In this method, the density of target nuclei and the solid angle of one telescope drop out in the ratio of breakup to elastic-scattering cross sections. One needs to determine only the solid angle of the other telescope, which is defined to a good approximation as the ratio of the area of the backward slit aperture to the distance between the center of the slit to the center of the target. This method was used for all measured configurations. The angular acceptances and the solid angles varied between $\Delta\vartheta = 0.9°$, $\Delta\varphi = 4.1°$, and $\Delta\Omega = 0.4$ msr for the most forward and $\Delta\vartheta = 2.2°$, $\Delta\varphi = 2.8°$, and $\Delta\Omega = 1.46$ msr for the most backward telescopes. The telescope slit systems were adjusted with an accuracy of 0.1°. Similarly, the accuracy of aligning the beam with the scattering-chamber axis was about 0.1°.

The FPS and BPS configurations were measured by pairs of telescopes set at the angles ($\vartheta_1^{\rm lab} = 35.2°$, $\varphi_1^{\rm lab} = 0.0°$, $\vartheta_2^{\rm lab} = 35.2°$, $\varphi_2^{\rm lab} = 180.0°$) and (75.4°, 0.0°, 75.4°, 180.0°), respectively. Two pairs of telescopes were used in case of the SSS configuration: (54.0°, 0.0°, 54.0°, 120.0°) and (50.0°, 60.0°, 54.0°, 180.0°).

The electronics system was designed so as to select and process two kinds of events: coincidences between any two telescopes and single events with a rate reduced by a factor of 1000 to a level acceptable for the data-acquisition system. In the energy-calibration measurement, single events only were collected. In order to accept an event, the coincidence between $\Delta E$ and $E$ detectors in a given telescope was required. Next, a given telescope had to be in coincidence with any other telescope (in the case of coincident events) or with the cyclotron radio-frequency (rf) signal (in the case of single events). The charge-sensitive analog-to-digital-converters (ADC's) integrated pulses coming directly from the photomultipliers within the duration of the gate signal individually synchronized to the leading edge of the pulse. The time measurement was referenced to the rf signal. The count rate of scintillator pulses was about 200 000 per second for the forward detectors and 50 000 per second for the backward ones.

The electronics system allowed also for a simultaneous measurement of purely random coincidences. This was achieved by setting the coincidence-gate width by about 30% larger than the time gap between the neighboring beam bursts. Two kinds of events were recorded: coincidences between particles originating from the very same burst and those from subsequent bursts. In the first case, ''true'' coincidences together with ''random'' ones (the so-called ''true + random'' coincidences) were collected. In the second case ''random'' coincidences only could be collected (the so-called ''purely random'' coincidences).

The digital information from the ADC, TDC, and scaler units was read by a CAMAC-based front-end processor connected via ETHERNET to the $\mu$VAX back-end computer. Each valid event consisted of a pattern word and digitized charges and times measured with respect to the rf signal. The pattern word contained coded information about the spin state of the beam and identified those detectors which had fired. The event rate reached a value of up to 1000 per second.

### B. Data analysis

Only about 1% of the events collected are due to the breakup process of interest. ''True'' events were selected in several steps: by applying particle identification, making use of timing information, and confronting them with kinematical conditions.

The procedure of event selection from raw data was preceded by energy and time calibrations. Energy calibration was achieved in dedicated measurements. A mixture of deuterium and hydrogen was used as a target throughout the energy-calibration measurements. A set of calibration points was established for each telescope by changing its angular position, which corresponds to the selected values of the energy of elastically scattered protons in the $^2{\rm H}(p,p)^2{\rm H}$ and $^1{\rm H}(p,p)^1{\rm H}$ scattering. Additionally, in front of telescopes measuring the FPS configuration, removable energy degraders were mounted. The reason was a geometrical limitation in the scattering chamber, which did not allow us to measure the calibration points with energies low enough. Changes of the detector angular position caused variations of its load (counting rate) and, consequently, of the detector gain. In order to eliminate this effect, light-emitting diodes (LED's) were used. Measured shifts of the LED peak in the pulse-height spectrum were used for correction of the proton-peak position. Figure 3 shows a typical distribution of the calibration points. Open and solid circles represent the measurements performed with and without energy degraders, respectively. The solid line in the picture is a quadratic fit to the data.

The time-of-flight spectrum of each detector contains two peaks (Fig. 4 in Ref. [3]) which are separated by the time interval between two subsequent beam bursts: 61.7 ns. These two lines were used for internal calibration of the TDC spectra. The linearity of TDC's was checked by applying known delays to the STOP signal and found to be sufficient in the time range of interest.

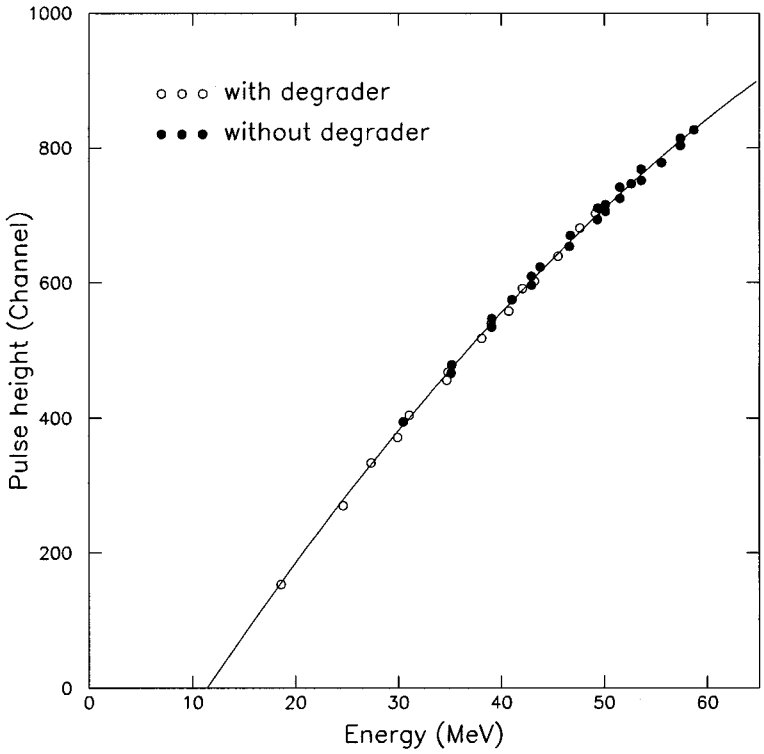


FIG. 3. Energy-pulse height relation. The solid line is the parabola fitted to the calibration points.

The standard $\Delta E$-$E$ method of particle identification applied to both coincident telescopes allowed us to reject typically about 90% of unwanted events (for details see Ref. [3]).

The whole data analysis was made separately for the above mentioned ''true+random'' and ''purely random'' events. The results of the applied subtraction procedure (described in detail in Ref. [3]) were the final distributions containing only ''true'' events.

The distribution of the time differences between the detection of two particles which start simultaneously (e.g., true coincidences of particles originating in a breakup reaction) is given by the time-of-flight differences. In contrast to that, this time-difference distribution for accidental coincidences is given by a convolution of the time-of-flight differences and the intensity distribution of the beam burst. Using this fact one can significantly improve the ratio of true-to-random coincidences. For each breakup event the time difference calculated using times $\Delta T_{\text{time}}=t_1-t_2$ is identical to such calculated using energies $\Delta T_{\text{energy}}=l_1\sqrt{m_1/2E_1}-l_2\sqrt{m_2/2E_2}$, where $t_1,t_2$ and $E_1,E_2$ are times and energies measured by two detectors in coincidence and $m_1,m_2$ and $l_1,l_2$ denote masses and flight paths of the particles under consideration. Thus, in an ideal case, when the time resolution of the apparatus is considerably better than the width of the proton beam burst, one can expect a sharp peak around zero in the spectrum $\Delta T\equiv\Delta T_{\text{energy}}-\Delta T_{\text{time}}$ caused by the breakup events, which ''sits'' on the broad bump resulting from random coincidences. In a real situation, two effects disturb the above picture. The first is the discriminator ''walk'' effect. Second, owing to the calibration procedure, the measured pulse heights in the $E$ detectors correspond to energies of protons emerging from the reaction; all the energy losses (first of all in the $\Delta E$ detectors) are already compensated for. Therefore, the $\Delta T_{\text{energy}}$ function gives the distorted time-difference distribution. Consequently, the two-dimensional spectrum of proton-proton coincidences, where $\Delta T_{\text{energy}}$ is plotted against $\Delta T_{\text{time}}$, contains events grouped around the curved (instead of straight) line corresponding to the $\Delta T_{\text{energy}}=\Delta T_{\text{time}}$ condition. A shape of this line was found by fitting of the third-order polynomial to a very well visible sharp ''ridge'' composed of ''true'' coincidences (Fig. 4). For each event the distance from this line was calculated and used for construction of the corrected $\Delta T$ spectrum. Figure 5 shows such a spectrum: Part (a) contains ''true + random'' coincidences, part (b) ''purely random'' coincidences, and part (c) the difference of them. From the last spectrum it was found that the intrinsic time resolution of the detecting system was of the order of 300 ps FWHM. By selecting a time window in this spectrum, a considerable amount of random coincidences (about 30%) is rejected in the evaluation of the final distributions.

The above-described filtering procedures rejected about 93% of accidental events. The remaining events are plotted as an energy coincidence spectrum (Fig. 6): part (a) contains the ''true+random'' events and part (b) the ''purely random'' ones. The coincidences of protons originating in the breakup reaction form a narrow band around the three-body kinematical curve calculated for a ''pointlike'' experimental geometry [solid line in Fig. 6(a)]. The width of this band is given by the dimensions of the beam, the target, and the apertures of the telescope slit system, as well as by the detector energy resolution. The kinematical condition was used for a further reduction of accidentals: The final subtraction of random coincidences measured was done only for a region around kinematical curve. In order to determine this region tight (and still safe) in a reproducible way, the following procedure was applied. The energies $E_1$ and $E_2$ of each event were transformed into two new variables $D$ and $S$, where

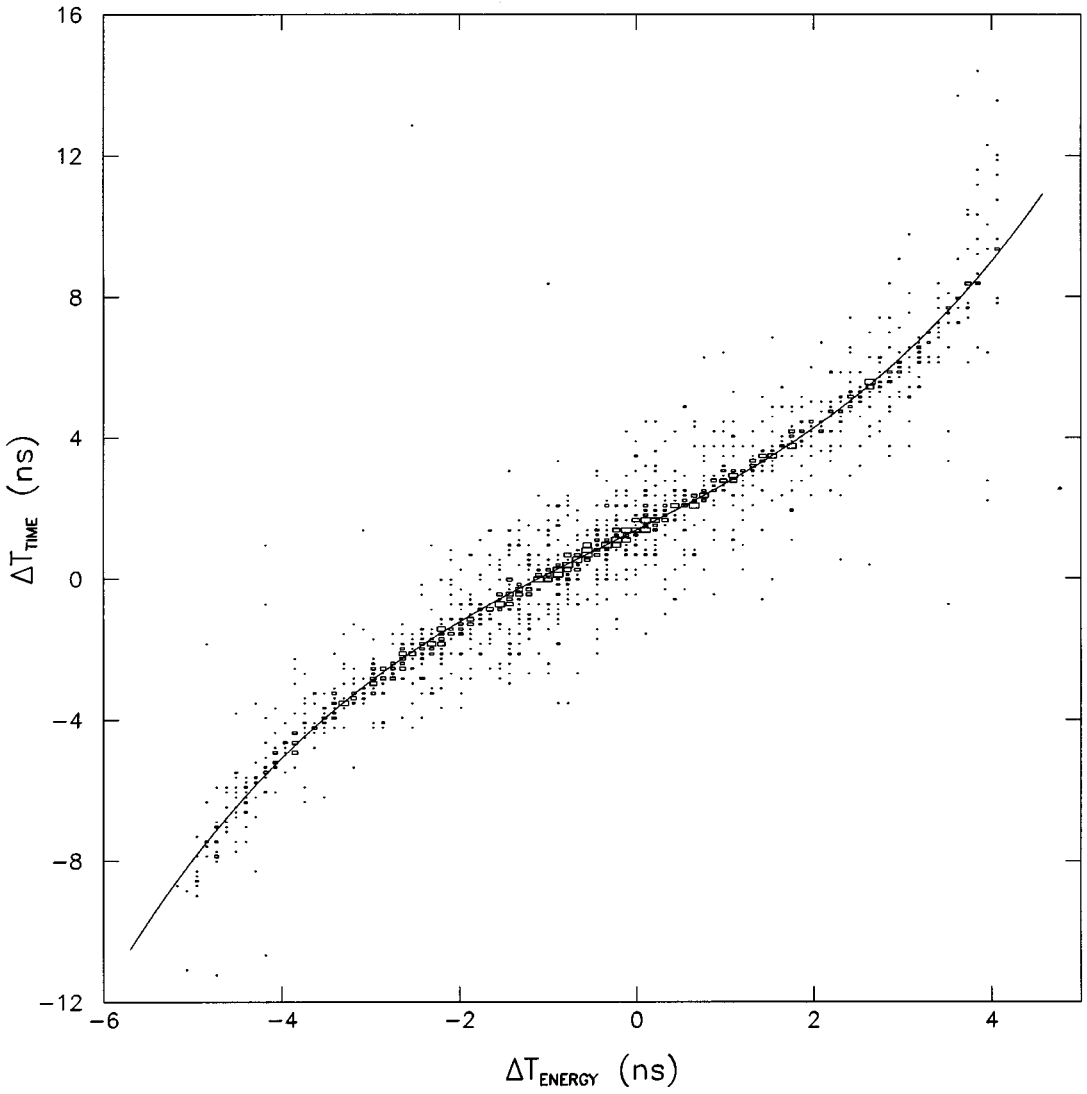


FIG. 4. Two-dimensional spectrum of proton-proton coincidences. The time-of-flight difference calculated from energies $\Delta T_{\text{energy}}$ is plotted versus $\Delta T_{\text{time}}$ measured directly. The third-order polynomial, fitted to the ''ridge'' of the breakup events, is shown.

$D$ is a distance of a point $(E_1,E_2)$ to the calculated kinematical curve on the $E_2$-$E_1$ plane and $S$ is the value of the arc length along the kinematical curve at the point where the line normal to the kinematics through the point $(E_1,E_2)$ crosses the kinematical curve. The zero value of the arc-length coordinate, $S=0$, was defined at the crossing point between the kinematical curve and the $E_1$ axis. The resulting spectrum for ''true+random'' events is shown in Fig. 7(a). The breakup events are seen now as a straight band around the line $D=0$. The projection onto the $D$ axis results in a spectrum shown in Fig. 7(b): There, ''true'' coincidences are included only, since the channel-by-channel subtraction of ''purely random'' coincidences was already performed. The breakup events appear now in a pronounced peak centered at $D=0$. Such projections were performed for different $S$ ranges, which allowed us to take into account changes of the width and of the position of the breakup locus. The width of the kinematical $D$ window was conservatively set at $\pm 4$ standard deviations of the peak.

After passing through the described filters, the events were projected onto calculated for a ''pointlike'' experimental geometry kinematical curve. To this end a set of points lying on the kinematics and being at a 2-MeV-arc-length distance from one another was chosen. Next, each event was ''ascribed'' to the nearest point. This projection resulted in one-dimensional spectra of coincidences as a function of the arc length along the kinematics. The absolute normalization of the cross section was made with the help of accurate $pd$ elastic-scattering data at 65 MeV measured by Shimizu *et al.* [20] and using the elastic events measured simultaneously with the breakup events. The dependences on the beam and on the target characteristics, as well as on the solid angle of the one of the coincident telescopes, are the same for both breakup and elastic-scattering cross section expressions. In result, the differential cross section is given by the formula

$$\frac{d^5\sigma_{\text{br}}}{d\Omega_1 d\Omega_2 dS}(S,\Omega_1,\Omega_2) = \frac{d^2\sigma_{\text{el}}}{d\Omega_1}(\Omega_1)\frac{N_{\text{br}}(S,\Omega_1,\Omega_2)}{N_{\text{el}}(\Omega_1)}\frac{1}{\Delta\Omega_2\Delta S}, \quad (1)$$

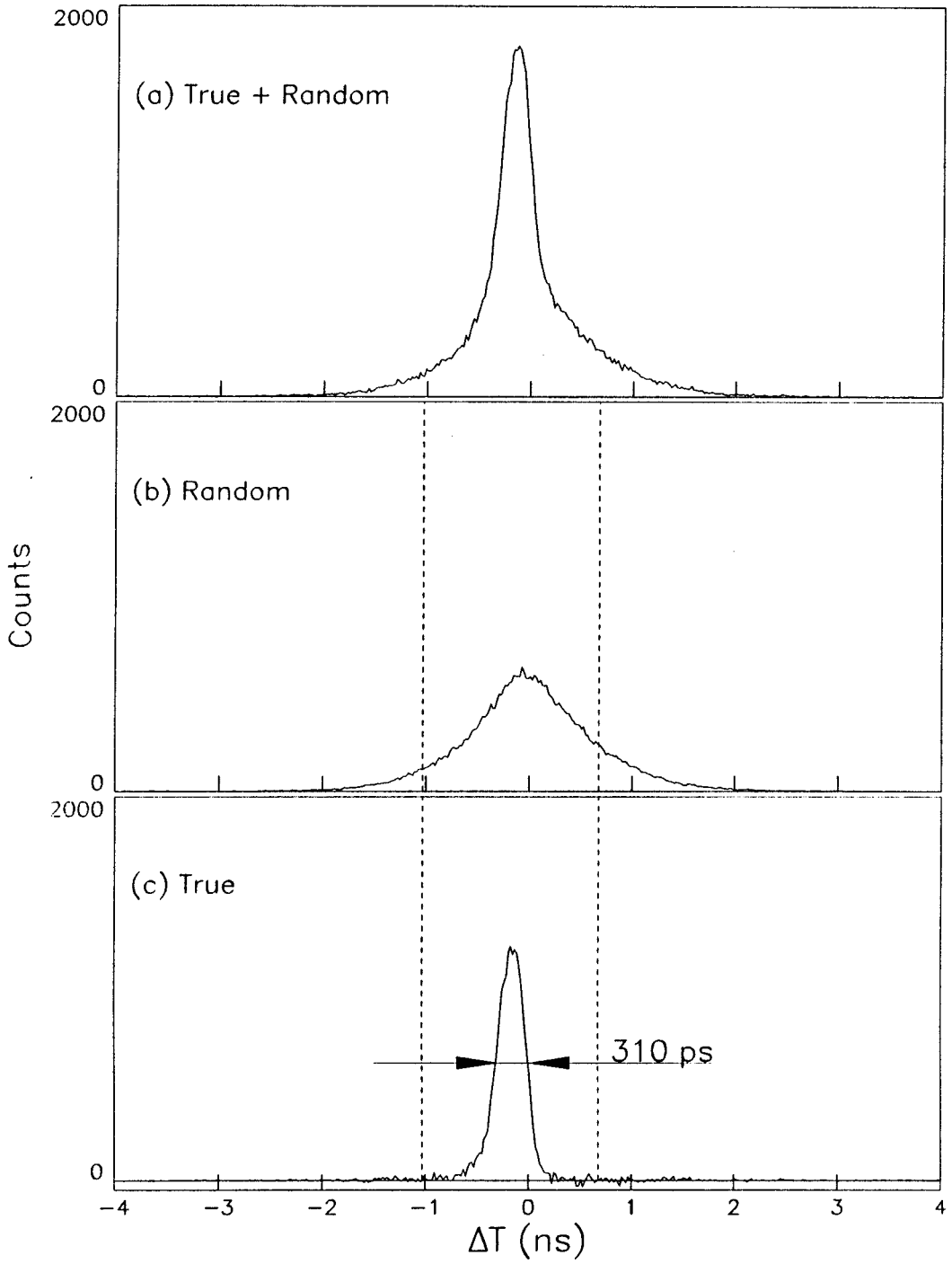


FIG. 5. Corrected time-difference $\Delta T$ spectra of coincidence events: (a) ''true+random'' events, (b) ''purely random'' events, and (c) ''true'' events obtained by subtracting (b) from (a). The vertical lines indicate the time window used in the evaluation of the cross section.

where $N_{\mathrm{br}}$ is the number of breakup events registered at detector angles $\Omega_1$ and $\Omega_2$ and projected into the $\Delta S$-wide arc-length bin centered at $S$. Here $\Omega_i=(\vartheta_i,\varphi_i)$ are the polar and azimuthal coordinates of the $i$th detector, $\Delta\Omega_i$ being its solid angle. $N_{\mathrm{el}}$ is the number of elastically scattered particles at $\Omega_1$. Events corresponding to different polarization states of the beam were summed up. Both particles, protons and deuterons, can be used for the determination of the $N_{\mathrm{el}}$. Figure 8 shows typical spectra of elastically scattered protons (a) and recoiled deuterons (b). The shape of the well-pronounced peaks was assumed to be a Gaussian function. For deuterons, besides a Gaussian, the constant background and the exponent convoluted with the Gaussian of the peak were also fitted. This convolution is assumed to represent the low-energy tail due to multiple scattering effects of the final particles in the gas, the target windows, and the collimator. In the case of the BPS configuration, the cross section normalization was obtained using the peak of the elastically scattered protons. The proton spectrum contains, in addition to the above-mentioned structures, protons originating in the

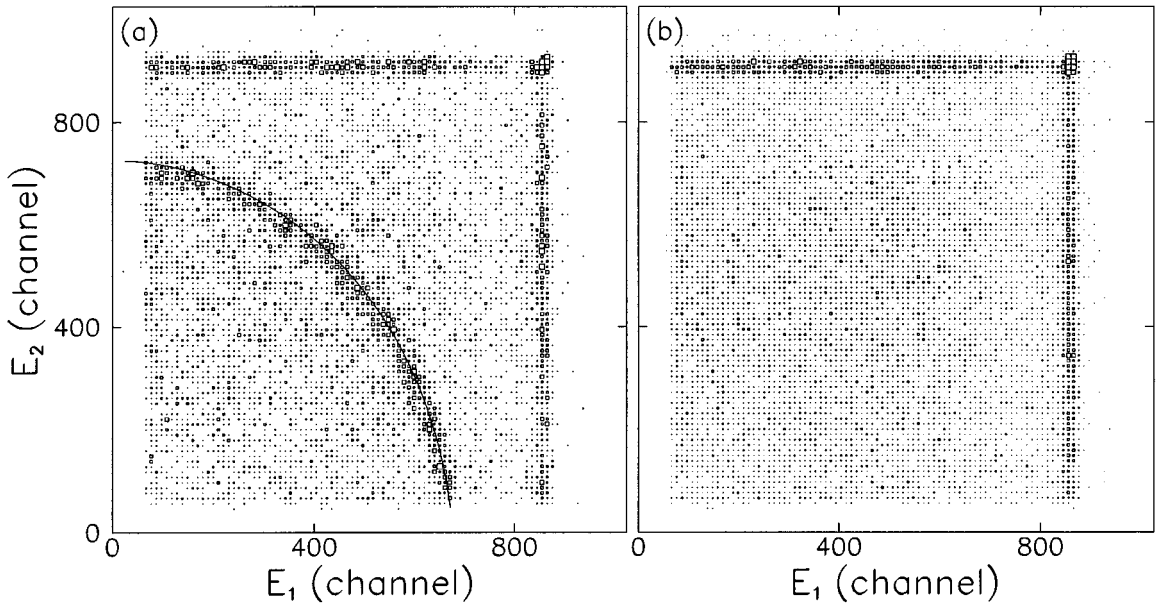


FIG. 6. $E_2$-$E_1$ spectrum of (a) ''true+random'' and (b) ''purely random'' proton-proton coincidences for the SSS configuration. Panel (a) contains the kinematical curve calculated for a ''pointlike'' experimental geometry.

inclusive breakup reaction; the shape of the inclusive spectrum was calculated theoretically. The $N_{\rm el}$ was found by summing up the Gaussain peak and the low-energy tail caused by multiple scattering effects in the energy interval corresponding to the width of the kinematical $D$ window described in the previous paragraph (i.e., also inside $\pm 4$ standard deviations of the peak).

The spectra of coincidences were obtained separately for both signs of the proton-beam polarization. In the case of the FPS and BPS configurations, the vector-analyzing power was calculated in the following way:

$$A_y(S)=\frac{1}{P_y}\frac{N_+(S)-N_-(S)}{N_+(S)+N_-(S)}, \tag{2}$$

where $P_y$ is the initial proton-beam polarization, and $N_-(S)$ and $N_+(S)$ are the numbers of events falling in a given $S$ bin for ''$-$'' and ''$+$'' states of the beam polarization, respectively. The SSS configuration was measured by two pairs of telescopes, and hence the ''superratio'' method was used:

$$A_y(S)=\frac{1}{P_y}\frac{r-1}{r+1}, \quad r^2=\frac{N_+^1(S)N_-^2(S)}{N_-^1(S)N_+^2(S)}. \tag{3}$$

The superscripts 1 and 2 correspond to the first and second pairs of telescopes, respectively. The charge collected in the Faraday cup was almost identical for both polarization states, and therefore the coincidence spectra had not to be normalized. The proton beam polarization was measured by the beam polarimeter. The ''superratio'' technique was used also here:

$$P_y=\frac{1}{A_y}\frac{r-1}{r+1}, \quad r^2=\frac{N_+^L N_-^R}{N_-^L N_+^R}, \tag{4}$$

where the value of the analyzing power $A_y=0.9985\pm 0.0015$ for the $^{12}\mathrm{C}(\vec{p},p)^{12}\mathrm{C}$ elastic scattering was taken from Ref. [18]. The superscripts $L$ and $R$ denote ''left'' and ''right'' detectors, respectively.

### C. Experimental uncertainties

In this section various effects contributing to the total error of the results are discussed in more detail. Table I summarizes the estimated values of the various contributions.

The statistical error depends on the number of ''true'' coincidences registered by the detectors and on the signal-to-background ratio, i.e., the true-to-random ratio. Despite optimizing the beam current and the small coincidence time window as well as the elaborated off-line reduction procedure, the amount of random coincidences remained considerable. The statistical uncertainty of single experimental points varied between 0.8% and 4.7% for the cross section and between 0.009 and 0.100 for $A_y$.

#### *1. Energy calibration*

One of the most important contributions to the total systematic error originates from the inaccuracy of the energy calibration of the detectors. Most of the effects responsible for the energy-calibration uncertainty can be related to the gain shifts caused by the strong variations of the counting rate during the calibration measurements. The applied corrections using the reference LED pulses were very useful, but could not eliminate the effects totally. Some uncertainty is also due to the difficulty of assigning energies to the peaks in the single-energy spectra. The influences of the uncertainty of the energy calibration on the experimental observables were estimated in the following way. The parameters of the channel-energy curve were varied within their error bounds (one standard deviation) and the event evaluation procedure was repeated. It was assumed that the error due to

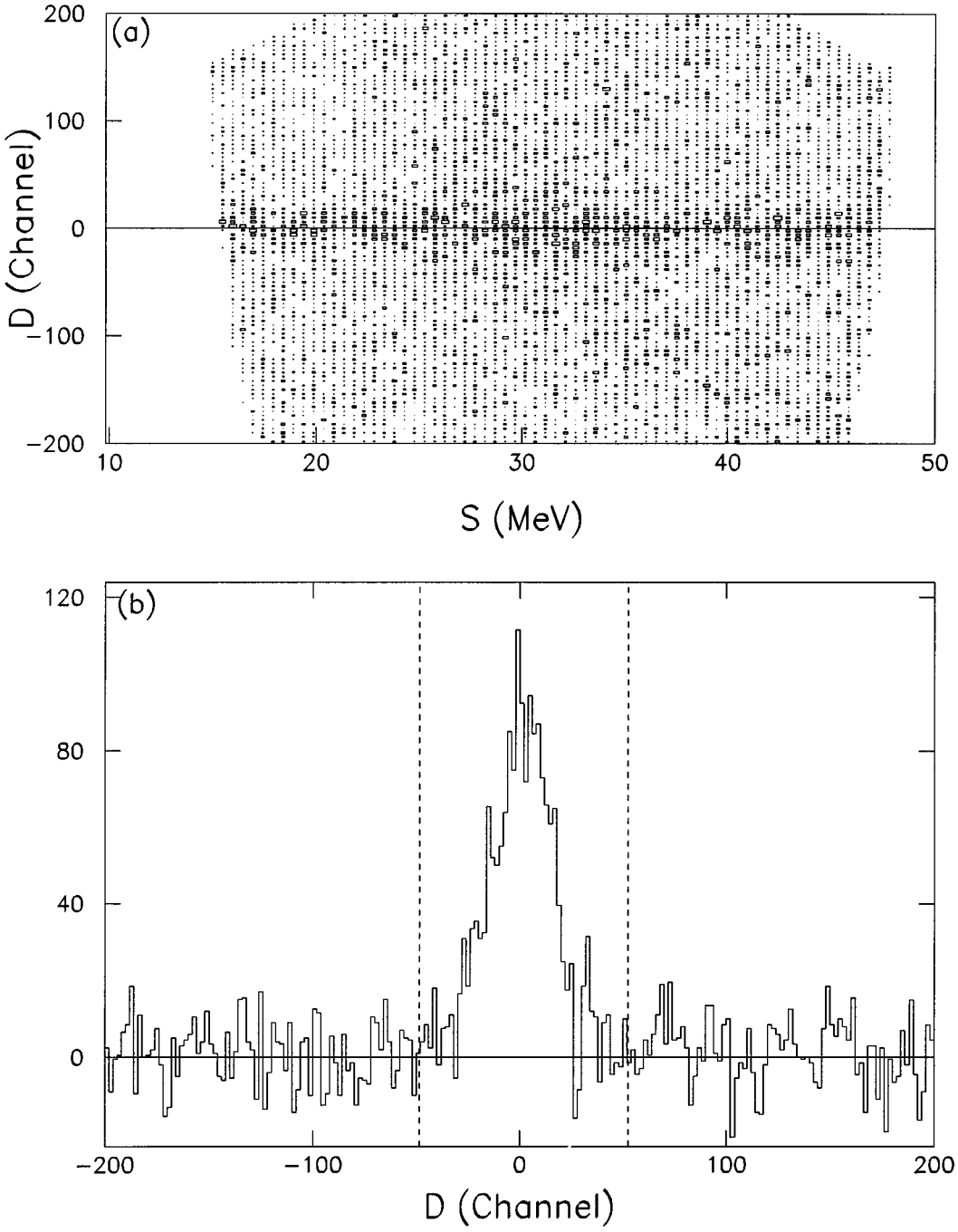


FIG. 7. (a) Transformed energy coincidence spectrum. $S$ is the arc length along the kinematical curve, and $D$ is the distance of an event from this curve. (b) Projection of the spectrum (a) onto the ordinate axis. Vertical lines indicate a window within which the breakup locus is included ($\pm 4$ standard deviations of the peak).

the energy-calibration uncertainty is equal to one standard deviation of the variation of experimental points. In extreme cases this error reached the value of 5% for the cross section and 0.025 for the analyzing power.

#### *2. Angle determination*

The mechanical construction of the scattering chamber allowed us to set the telescope angles with an accuracy better than 0.1°. The proton beam direction was aligned with the chamber axis also with an accuracy of 0.1°. These inaccuracies affect the experimental observables since they are angle dependent. The upper limit of this influence was estimated by calculating the theoretical observables with shifted angles. The largest effects were found in the FPS configuration. They depend on arc length $S$ and reach, in the extreme case, 4.5% and 0.007 for the cross section and $A_y$, respectively. In other configurations the deviations are generally smaller: 0.8%/0.003 and 2.5%/0.012 for the SSS and BPS configurations, respectively. The uncertainty of the angular settings is included in the systematic error of each measured point separately. The influence of the angular uncertainties on the cross-section normalization is described below.

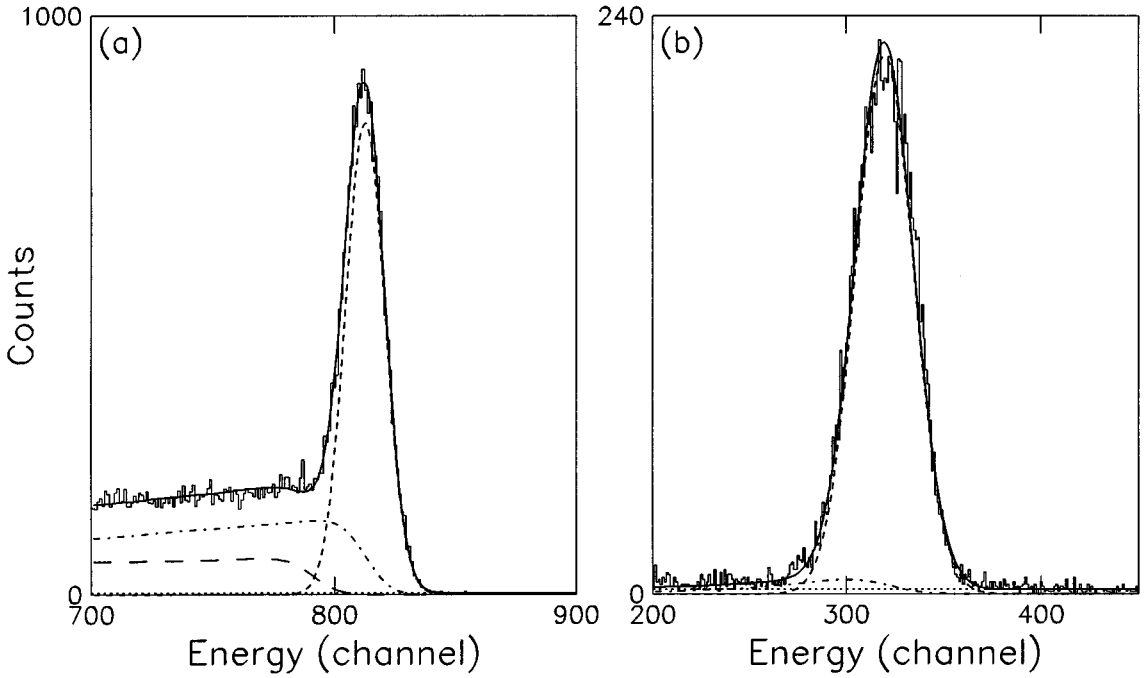


FIG. 8. Energy spectra of elastically scattered protons (a) and recoiled deuterons (b). The solid line represents the fit to the spectrum. The fitted function consists of a Gaussian function (dashed line), a constant background (dotted line), and an exponent convoluted with the Gaussian function (dash-dotted line). The long-dashed line in panel (a) represents the inclusive spectrum of breakup events, the shape of which was calculated theoretically and folded with the experimental energy resolution.

#### *3. Normalization*

This kind of error affects the cross section only. From Eq. (1) it can be seen that there are three potential sources of systematic errors: elastic-scattering cross section, solid angle $\Delta\Omega_2$, and the number of elastically scattered particles, $N_{\mathrm{el}}$. The error of the *pd* elastic-scattering cross section as given by the authors of [20] is about 1.6%. From the angular distribution of these data, it was deduced that the described above angular uncertainties affect the normalization error by about 0.5%.

The main difficulty in calculating the error of the solid angle is the uncertainty of the distance between the collimator aperture and the center of the target. It contributes 0.4% to the cross section error. The value of $N_{\mathrm{el}}$ is affected by the choice of summation limits. In the elastic-scattering spectrum shown in Fig. 8, a low-energy tail occurs which is due to slit scattering and multiple scattering effects in the target as could be demonstrated by a Monte Carlo simulation. Of course, the slit scattering affects the coincidence spectra, too. It was checked that increasing the width of the event summation windows from $\pm 4$ to $\pm 5$ standard deviations increases $N_{\mathrm{el}}$ by (1–1.5)% and the number of true coincidences by (1–2)%. Thus it was concluded that effects in the single and coincidence spectra compensate each other in the value of the breakup cross section to a large extent. The remaining effect was conservatively assumed to be about 1.0%. The total systematic uncertainty of the cross section normalization procedure is about 2.0%.

TABLE I. Summary of the experimental uncertainties.

| Source of error | Cross section (%) | Analyzing power (absolute) |
|---|---|---|
| Statistical | 0.8–4.7 | 0.009–0.100 |
| Energy calibration | 0.0–5.0 | 0.000–0.025 |
| Angular setting | 0.0–4.5 [a] | 0.000–0.012 [b] |
| Slit scattering | 1.0 | negligible |
| Solid angle | 0.4 | no influence |
| Beam polarization | no influence | 0.006 |
| Elastic cross section | 1.7 | no influence |
| Total systematic | 1.9–6.3 | 0.006–0.047 |

[a]For the SSS configuration: 0.0–0.8.
[b]For the SSS configuration: 0.000–0.001.

#### *4. Dead time and pileups*

Dead-time losses in the electronics and in the acquisition system were of the order of a few percent. Event processing in the CAMAC system and in the front-end computer yielded the biggest contribution to the dead-time losses. Since the counting rates of the elastic scattering and of the breakup reaction are very different, this would require a careful monitoring and measurement of the dead times for these processes independently. In order to avoid this, after the detection of any event, the inputs of *all* ADC's were inhibited until the event had been read. Hence the dead time was the same for both breakup coincidence events and the single events and dead-time corrections drop out from the formulas used to calculate the cross section and the analyzing power.

The probability of a pileup depends on the single detector counting rate. The load of the *E* detectors was about 200 000

per second for forward detectors and 50 000 per second for the backward ones. Because the total length of the detector signal was about 50 ns, the probability of a pileup reached about 1% at forward angles and 0.3% at backward angles. Decreasing the beam current by a factor of 3 did not reveal any visible effects in the shape of the cross section measured. The influence of pileup events on the final result was well below 0.2%.

#### *5. Analyzing power $A_y$*

The systematic uncertainty of $A_y$ stems mainly from the error associated with the initial beam polarization. This, in turn, is caused by the experimental error of the analyzing power of protons elastically scattered off $^{12}$C: 0.0015 [18]. The statistical error is negligible, and the error due to background subtraction in the polarimeter spectra was estimated to be 0.003. The total systematic uncertainty of $P_y$ was 0.0034.

## III. THEORY

The theoretical results presented in this work are based on rigorous solution of the $3N$ Faddeev equations using different realistic $NN$ interactions. In the following we give a short presentation of our formalism and numerical performance.

When only $NN$ interactions are active and neglecting the long-range Coulomb force, the Faddeev equations are solved for the $T$ operator:

$$T = tP + tPG_0T, \tag{5}$$

where $G_0$ is the free three-body propagator and $t$ is the two-body off-shell $t$ matrix. $P$ denotes a sum of cyclical and anticyclical permutations of three nucleons. After solving Eq. (5) the breakup-transition operator $U_0$ can be expressed as

$$U_0 = (1+P)T. \tag{6}$$

If the potential energy of the $3N$ system contains in addition to the pure $NN$ interaction also a term due to a three-nucleon force (3NF), we introduce the operator $t_4 = V_4 + V_4G_0t_4$, driven by the three-nucleon interaction $V_4$. Now in the transition operator $U_0$ a new term $T_4$ on top the $T$ appears. $T$ and $T_4$ fulfill the following set of coupled equations:

$$T = tP + tG_0T_4 + tPG_0T, \tag{7}$$

$$T_4 = (1+P)t_4 + (1+P)t_4G_0T. \tag{8}$$

These equations are solved in a perturbative approach in powers of $V_4$, and the different orders are then summed up by the Padé method. The breakup amplitude is then given by

$$U_0 = (1+P)T + T_4. \tag{9}$$

The physical content of Eqs. (5), (7), and (8) is revealed after iterating them. The resulting multiple scattering series describe contributions from scattering processes where three nucleons interact with two- or three-body forces with free propagation in between. For more details of the theoretical formulation and the numerical performance, we refer to [1,2,21,22], and references therein.

We solved Eq. (5) using the following recently updated high quality $NN$ interactions: Argonne $v_{18}$ (AV18) [23], CD Bonn [24], and Nijmegen 93, I and II [25]. All these interactions are charge dependent in the isospin $T=1$ states, having thus inherently built in a difference in the $^1S_0$ force component for $np$, $pp$, and $nn$ systems. Contrary to the older and charge-independent potentials (e.g., those used in Ref. [3]), they are practically on-shell equivalent and describe the $2N$ data with impressive good quality characterized by $\chi^2 \approx 1$ per degree of freedom.

In order to get some insight into possible 3NF effects, we included in the calculation also the Tucson-Melbourne (TM) three-nucleon force [26,27] together with the charge-independent Bonn B $2N$ one [28]. From our previous study [2] we know that effects of this 3NF depend strongly on the value of the cutoff parameter $\Lambda_\pi$ appearing in the $\pi NN$ form factor. In the present calculations we used the ''recommended'' [27] value for this parameter, $\Lambda_\pi = 5.8\mu$ ($\mu = 139.6$ MeV). But in this case, the binding energy of the triton when the Bonn B potential and the TM-3NF act is overestimated. To get a proper binding of the triton, and value of $\Lambda_\pi = 4.55\mu$ should be used. Such a decrease of $\Lambda_\pi$ would reduce the effects of the TM-3NF and make them significantly smaller.

In all calculations performed with $2N$ interactions only, we included all $3N$ states with total angular momenta of the two-nucleon subsystem, $j \leqslant 3$, which was checked to be sufficient for the energy of 65 MeV. For the calculation with TM-3NF due to computer limitations, we restricted them to $j \leqslant 2$. Surely this is not sufficient, but we think that the resulting 3NF effects give some orientation on the expected magnitude of the real 3NF effects at this energy.

The theoretical calculations were performed for point geometry. In reality, the telescope slit systems had a finite angular acceptances in both angles $\vartheta$ and $\varphi$, and in addition the extended target was used. Moreover, the detectors introduced some finite energy resolutions. The influence of these experimental conditions as compared to the point-geometry results was investigated with a code based on the Monte Carlo method. Using this code, the most important experimental ''averaging'' effects on the theoretical predictions were studied. When compared with point-geometry results, they provided a measure of the influence of instrumental effects on the calculated observables. We found that for our experimental conditions these effects are negligible in the case of SSS and FPS configurations. In the case of the BPS configuration, they are important and influence significantly the cross section (Fig. 9).

At the energy of our experiment, relativistic effects are visible already at the level of kinematics as can be seen by comparing directly the point-geometry loci calculated using relativistic and nonrelativistic expressions. While our strictly nonrelativistic theory delivers the observables along the nonrelativistic locus, the experimental data lie surely along the relativistic one. Thus the question arises how one should compare theory with experiment. The best solution would be to have a fully relativistic theoretical framework, which, however, is not available at the moment. Therefore the approximate procedure, discussed in detail in Ref. [3], was ap-

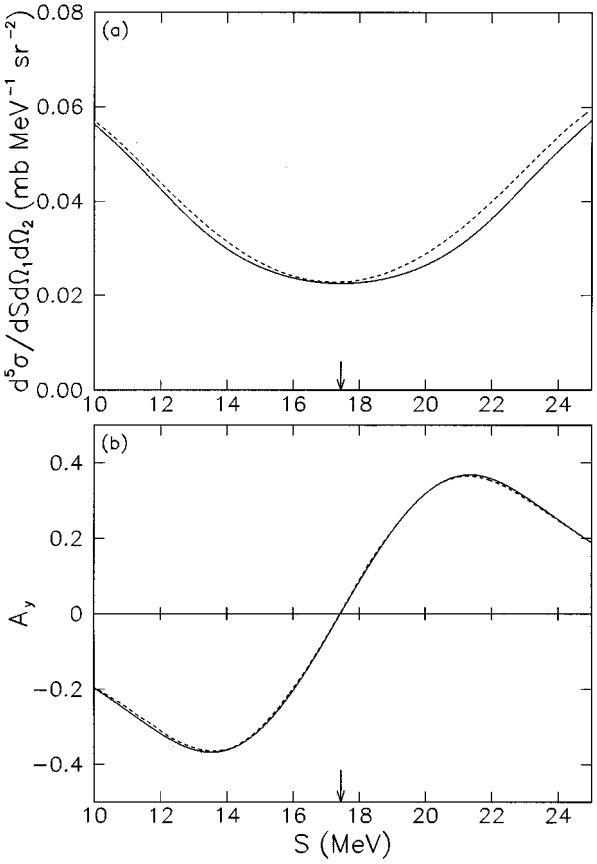


FIG. 9. Influence of the instrumental averaging on the cross section and the analyzing power calculated with the Bonn B potential in case of the BPS configuration. The solid line shows the results of the calculations with ''pointlike'' geometry and with ignored energy resolution of the detectors. The dashed line presents the theoretical predictions in which the experimental averaging is included. The obtained shape asymmetry is caused by the different angular acceptances of the coincident telescopes.

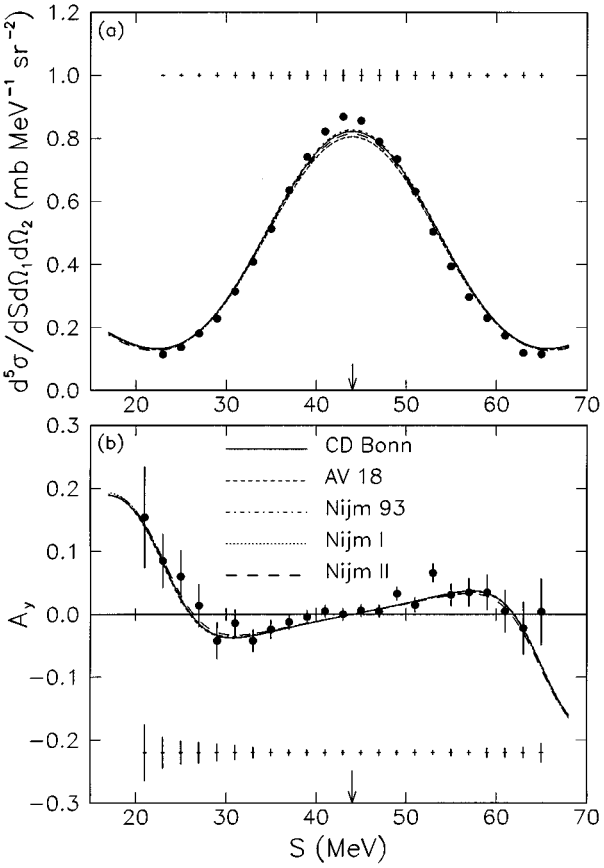


FIG. 10. Experimental cross-section and analyzing-power $A_y$ distributions (black dots) for the forward plane star (FPS) configuration ( $\vartheta_1^{\rm lab}=35.2°$, $\vartheta_2^{\rm lab}=35.2°$, and $\varphi_{12}^{\rm lab}=180°$). Error bars represent the statistical errors. The total systematic errors are shown for each point separately above or below the distributions. The curves result from the calculations performed with the use of five charge-dependent *NN* potentials: CD Bonn (solid line), AV18 (dashed line), Nijmegen 93 (dash-dotted line), I (dotted line), and II (long-dashed line). The arrows indicate the position of the exact FPS point.

plied. This procedure relates uniquely the arc length parametrization of the relativistic and nonrelativistic kinematical curves.

## IV. EXPERIMENTAL RESULTS AND COMPARISON WITH THEORETICAL CALCULATIONS

Both experimental results and theoretical calculations are presented as a function of the arc length $S$ of the kinematical curve. The experimental results are shown in Figs. 10–15 by black dots in which error bars represent the statistical error. The total systematic errors are shown above or below data separately for each point. For safety, the cross-section values at the ends of the measured arc-length interval were rejected as they could be affected by the neighborhood of the low-energy thresholds of detectors.

As a result of parity conservation, the cross sections (analyzing powers $A_y$) measured by the FPS and BPS detector settings have to be symmetric (antisymmetric) with respect to the exact kinematical points (indicated by arrows in Figs. 9–15). Indeed the experimental data exhibit that symmetry nicely. In the case of SSS, that symmetry is present only in the cross section, but not in $A_y$, because the spin axis did not coincide with the symmetry plane of the detectors in that configuration.

The experimental cross section in the FPS configuration is dominated by the prominent bump around $S=44$ Mev (Fig. 10). The nature of this bump can be understood as a consequence of the quasifree-scattering (QFS) process which affects this configuration. Generally, the differential cross section is very well described by the theory. However, the value of the cross section in the FPS point is underestimated in calculations by about 6% for all *NN*-interaction models used, while the systematic error is about 2%. Also, the predicted width of the observed peak is larger than the experimental one by about 7%. A particularly nice agreement between experiment and theory for the vector-analyzing power is worth to note. The theoretical curves calculated with different potentials differ only slightly from one another.

Despite using extremely thin $\Delta E$ plastic detectors, only 12 MeV of the arc length was available to the experiment in the BPS configuration (Fig. 11). As has already been explained, in this particular case, the instrumental averaging effects are significant. Upon their inclusion, a good agree-

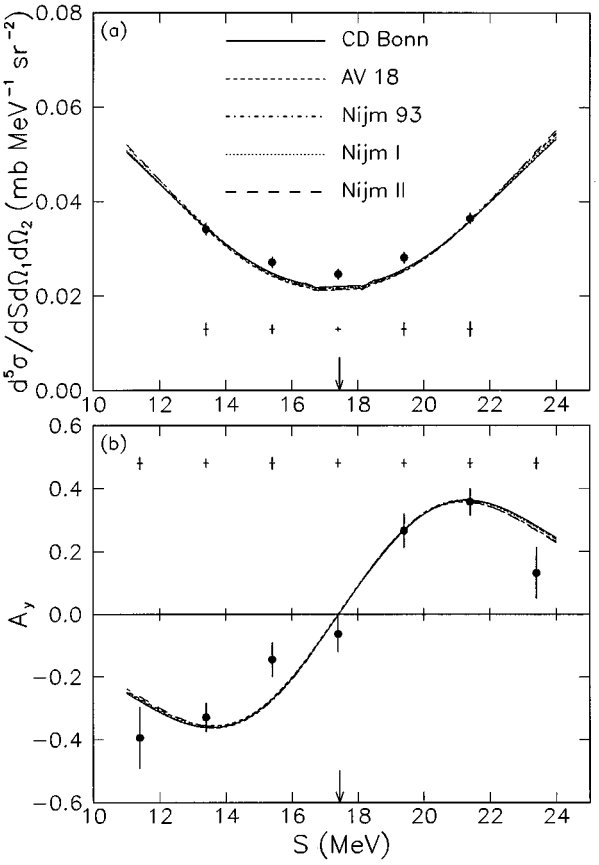


FIG. 11. Same as Fig. 10, but for the BPS configuration (75.4°, 75.4°, 180°).

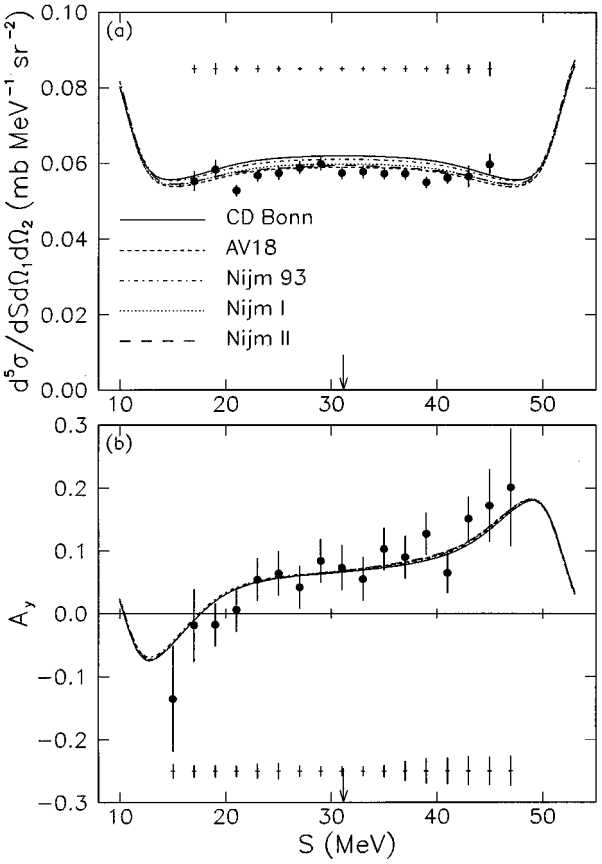


FIG. 12. Same as Fig. 10, but for the SSS configuration (54.0°, 54.0°, 120°).

ment with theory was achieved for the cross section. Only in the range of the BPS condition does the theory underestimate the cross section by about 10%. The same statement for the vector-analyzing power $A_y$ is not yet justified, because the experimental errors are still quite large. As in the case of the FPS configuration, the results of the theoretical calculations for all $NN$ potentials used practically coincide.

The measurement in the symmetric space star (SSS) configuration was the main aim of the presented experiment. This configuration was expected to be particularly suitable to trace $3N$-force effects in the continuum [17]. A comparison of the currently measured cross section with rigorous Faddeev calculations involving realistic potentials does not confirm those expectations (Fig. 12). The cross sections calculated using different $NN$ potentials differ from one another by up to 5% and tend to overestimate the experimental data. The poorest agreement was achieved for the CD Bonn potential (up to about 6%; in this case the systematic errors are of the order of 1%), which performed well in the collinearity configurations [3]. The agreement between theory and experiment seems to be better in case of $A_y$, but the experimental errors are still too large to draw a definite conclusion.

In order to shed more light into the nature of discrepancies between experiment and theory, especially the ones observed in the SSS configuration, the Faddeev calculations were performed with a $3N$ force included in a rigorous way. The size of $3N$-force effects can be estimated by comparing the observables obtained with and without the $3N$ force in the truncated angular momentum space $j_{\max}=2$.

Figure 13 shows such a comparison for the FPS configuration. Taking the overestimated ($\Lambda_\pi=5.8\mu$) $3N$ force into account decreases the cross section. This behavior makes the agreement between theory and experiment even worse. In the case of $\Lambda_\pi=4.55\mu$, the $3N$-force effects are negligible.

Similarly, the $3N$-force effects in case of the BPS configuration are negligible for the ''correct'' cutoff parameter (Fig. 14). Even the overestimated effects increase the cross section only by 6% in the BPS point.

The case of the SSS configuration is presented in Fig. 15. The effects of the $3N$ force included in the cross section are significant: about 3% for $\Lambda_\pi=4.55\mu$ and about 15% for $\Lambda_\pi=5.8\mu$. Unfortunately, the correction goes in the wrong direction when the calculations are compared with the experimental data. In the case of $A_y$, the effects are smaller. Again, the trend of the changes is wrong.

## V. SUMMARY

Kinematically complete measurements of the deuteron breakup reaction induced by transversally polarized protons at the laboratory energy of 65 MeV were performed. Both the differential cross section and the vector-analyzing power were studied for three star configurations: symmetric forward plane star (FPS), symmetric backward plane star (BPS), and symmetric space star (SSS). The results of the experiment were compared with the rigorous $3N$ calculations involving five charge-dependent $2N$ potentials: AV18, CD Bonn, Nijmegen 93, Nijmegen I, and Nijmegen II. A comparison

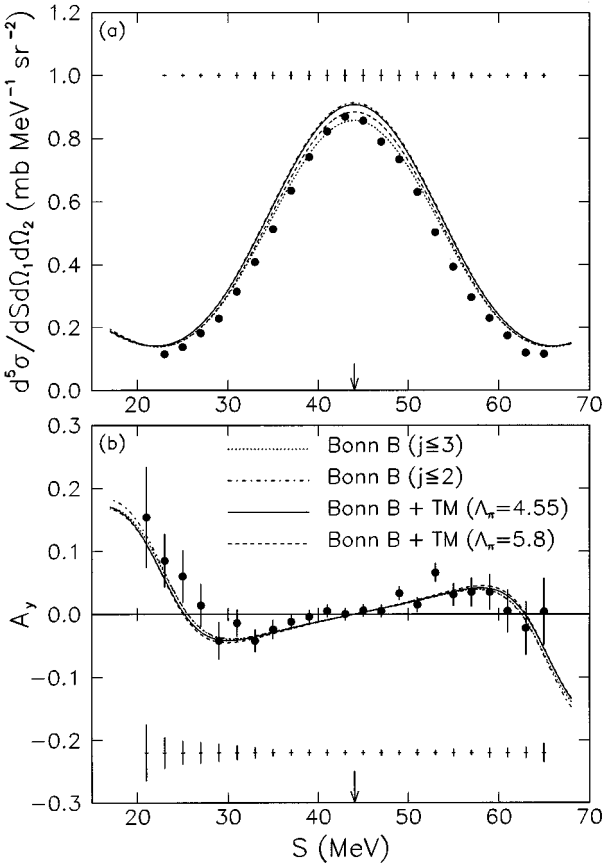


FIG. 13. Experimental cross-section and analyzing-power $A_y$ distributions (black dots) compared with the theoretical predictions with (solid and dashed lines for $\Lambda_\pi = 4.55\mu$ and $5.8\mu$, respectively) and without (dash-dotted line) TM-3NF included into the dynamics of the $3N$ system for the FPS configuration. The charge-independent Bonn B potential is used as a $2N$ potential. The calculations are performed with $2N$ system angular momentum space limited to $j \leqslant 2$. For comparison, the dotted line shows the analogous calculations without the $3N$ force included with $j \leqslant 3$.

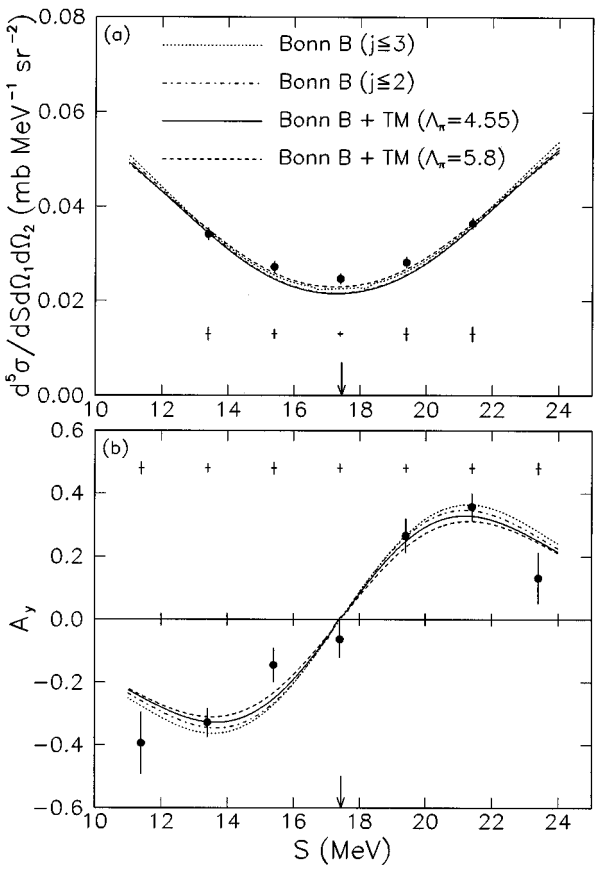


FIG. 14. Same as Fig. 13, but for the BPS configuration.

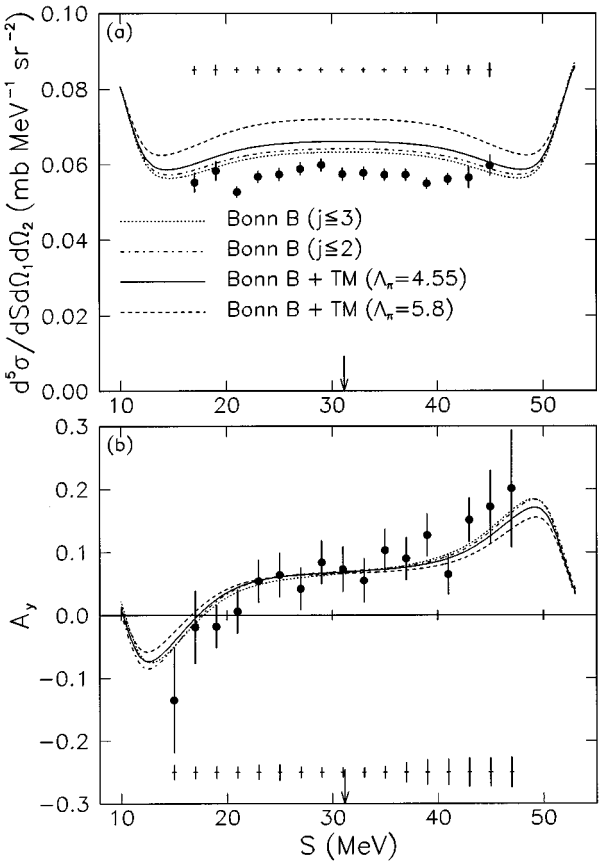


FIG. 15. Same as Fig. 13, but for the SSS configuration.

with rigorous calculations including a $3N$ force in the dynamics of the $3N$ system was also made. These calculations, with still limited angular momentum space, were based on the charge-independent Bonn B $2N$ potential and the Tucson-Melbourne $3N$ potential.

By examining the calculations without the $3N$ force, one can conclude that, in general, the experimental results and the theoretical predictions agree well. This is particularly true for the case of the analyzing power which is very well described by theory. However, there are also some minor disagreements. The theoretically calculated cross sections overestimate (SSS) or underestimate (FPS and BPS) experimental values by (6–10)%. The width of the theoretically calculated FPS peak is by about 7% larger than the experimental one.

In the comparison of the experimental results with the calculations including the $3N$ force, one notices that virtually no $3N$-force effects can be found in the case of the FPS and BPS configurations with a cutoff parameter $\Lambda_\pi = 4.55\mu$. In the case of the SSS configuration, this effect is visible, but small. When taking the cutoff parameter which overbinds the

triton, the $3N$-force effects are more significant (for the SSS configuration, an effect of about 15% in the cross section was found). But in almost all cases, the agreement between theory and experiment gets worse as compared to the calculations without the $3N$ force.

The reason for this phenomenon is not yet clear. On the one hand, the $3N$ potential (Tucson-Melbourne) may be wrong. The new versions of this potential (e.g., [30]) were not yet included in calculations. On the other hand, the Tucson-Melbourne $3N$ potential was not derived in the same theoretical framework as the Bonn B potential, making them to some extent incompatible. It would be interesting to find out how far this incompatibility is important by performing calculations with both $NN$ and $3N$ forces derived consistently in the same framework as, e.g., [29]. Such a work is underway.

The observed disagreement of the cross section values in the SSS configuration may be also caused by neglect of the Coulomb force. This possibility was indicated by a model calculation where the nucleon interaction was truncated to the $S$ waves only while the full Coulomb potential was included [31]. It should be stressed, however, that it is not yet clear whether the Coulomb effect will survive when the calculations are performed with a realistic nuclear interaction. In our earlier work [14] we suggested that the disagreement in the width of the FPS peak may be also caused by neglecting the Coulomb force. The measured analyzing powers $A_y$ agree, in general, better with the theory based on the 2N interaction only than do the cross sections, thus leaving less room for $3N$-force effects. On the other hand, higher partial waves ($j \geqslant 3$) are more important in $A_y$ than in the cross section, and so the presented calculations performed in the truncated angular momentum space ($j \leqslant 2$) should be extended to at least $j_{\max}=3$.

## ACKNOWLEDGMENTS

This work was supported by the Polish Committee for Scientific Research under Grant No. 2 P302 104 06 and by the Swiss National Foundation. The numerical calculations were performed on the CRAY Y-MP of the Höchstleistungsrechenzentrum in Jülich, Germany, on the NEC SX3 of the SCSC in Manno, Switzerland, and on the CONVEX C3820 of the ACK-Cyfronet in Cracow, Poland (Grant No. KBN/UJ/054/95).

[1] H. Witała, T. Cornelius, and W. Glöckle, Few-Body Syst. **3**, 123 (1988).

[2] D. Hüber, H. Witała, and W. Glöckle, Few-Body Syst. **14**, 171 (1993).

[3] M. Allet, K. Bodek, W. Hajdas, J. Lang, R. Müller, O. Naviliat-Cuncic, J. Sromicki, J. Zejma, L. Jarczyk, St. Kistryn, J. Smyrski, A. Strzałkowski, W. Glöckle, J. Golak, H. Witała, B. Dechant, J. Krug, and P. A. Schmelzbach, Phys. Rev. C **50**, 602 (1994).

[4] C. R. Howell, W. Tornow, H. R. Setze, R. T. Braun, D. E. Gonzales Trotter, C. D. Roper, R. S. Pedroni, S. M. Grimes, C. E. Brient, N. Al-Niemi, F. C. Goeckner, and G. Mertens, Few-Body Syst. **16**, 127 (1994).

[5] D. R. Tilley, H. R. Weller, and H. H. Hasan, Nucl. Phys. **A474**, 1 (1987).

[6] C. R. Howell, W. Tornow, I. Slaus, P. D. Felsher, M. L. Roberts, H. G. Pfützner, Anli Li, K. Murphy, R. L. Walter, J. M. Lambert, P. A. Treado, H. Witała, W. Glöckle, and T. Cornelius, Phys. Rev. Lett. **61**, 1565 (1988).

[7] M. Stephan, K. Bodek, J. Krug, W. Lübcke, S. Obermanns, H. Rühl, M. Steinke, D. Kamke, H. Witała, T. Cornelius, and W. Glöckle, Phys. Rev. C **39**, 2133 (1989).

[8] J. Strate, K. Geissdörfer, R. Lin, W. Bielmeier, J. Cub, A. Ebneth, E. Finckh, H. Friess, G. Fuchs, K. Gebhardt, and S. Schindler, Nucl. Phys. **A501**, 51 (1989).

[9] H. R. Setze, C. R. Howell, R. T. Braun, D. E. Gonzales Trotter, A. H. Hussein, C. D. Roper, F. Salinas, I. Slaus, W. Tornow, B. Vlahovic, R. L. Walter, G. Mertens, J. M. Lambert, and H. Witała, in Proceedings of the 14th International IUPAP Conference on Few-Body Problems in Physics, Williamsburg, Virginia, 1994, edited by F. Gross (CEBAF, Newport News, VA, 1994), p. 177.

[10] M. Karus, M. Buballa, J. Helten, B. Laumann, R. Melzer, P. Niessen, H. Oswald, G. Rauprich, J. Schulte-Uebbing, and H. Paetz gen. Schieck, Phys. Rev. C **31**, 1112 (1985).

[11] G. Rauprich, S. Lamaitre, P. Niessen, K. R. Nyga, R. Reckenfelderbäumer, L. Sydow, H. Paetz gen. Schieck, H. Witała, and W. Glöckle, Nucl. Phys. **A535**, 313 (1991).

[12] H. Shimizu, K. Imai, T. Matsusue, J. Shirai, R. Takashima, K. Nisimura, K. Hatanaka, T. Saito, and A. Okihana, Nucl. Phys. **A380**, 111 (1982).

[13] St. Kistryn, W. Hajdas, J. Lang, R. Müller, J. Balewski, K. Bodek, L. Jarczyk, B. Kamys, A. Strzałkowski, B. Dechant, J. Krug, W. Lübcke, H. Rühl, G. Spangardt, M. Steinke, M. Stephan, D. Kamke, H. Witała, T. Cornelius, W. Glöckle, and J. Golak, Nucl. Phys. **A548**, 49 (1992)

[14] M. Allet, K. Bodek, W. Hajdas, J. Lang, R. Müller, O. Naviliat-Cuncic, J. Sromicki, J. Zejma, L. Jarczyk, St. Kistryn, J. Smyrski, A. Strzałkowski, W. Glöckle, J. Golak, D. Hüber, H. Kamada, and H. Witała, Few-Body Syst. **20**, 27 (1996).

[15] J. Balewski, K. Bodek, L. Jarczyk, B. Kamys, St. Kistryn, A. Strzałkowski, W. Hajdas, R. Müller, B. Dechant, J. Krug, W. Lübcke, H. Rühl, G. Spangardt, M. Steinke, M. Stephan, D. Kamke, R. Henneck, H. Witała, W. Glöckle, and J. Golak, Nucl. Phys. **A581**, 131 (1995).

[16] L. M. Qin, W. Boeglin, D. Fritschi, J. Götz, J. Jourdan, G. Masson, S. Robinson, J. Sick, P. Trueb, M. Tuccillo, B. Zihlmann, H. Witała, J. Golak, W. Glöckle, and D. Hüber, Nucl. Phys. **A587**, 252 (1995).

[17] W. Meier and W. Glöcke, Phys. Lett. **138B**, 329 (1984).

[18] P. D. Eversheim, F. Hinterberger, U. Lahr, B. von Przewoski, J. Campbell, J. Götz, M. Hammans, R. Henneck, G. Masson, and I. Sick, Phys. Lett. B **234**, 253 (1990).

[19] J. E. Durisch, W. Neumann, and J. Rossel, Nucl. Instrum. Methods **80**, 1 (1970).

[20] H. Shimizu, K. Imai, N. Tamura, K. Nisimura, K. Hatanaka, T.

Saito, Y. Koike, and Y. Taniguchi, Nucl. Phys. **A382**, 242 (1982).
[21] W. Glöckle, *The Quantum Mechanical Few-Body Problem* (Springer-Verlag, Berlin, 1993).
[22] L. D. Faddeev, Sov. Phys. JETP **12**, 1014 (1961).
[23] R. B. Wiringa, U. G. J. Stoks, and R. Schiavilla, Phys. Rev. C **51**, 38 (1995).
[24] R. Machleidt (private communication).
[25] U. G. J. Stoks, R. A. M. Klomp, C. P. F. Terheggen, and J. J. de Swart, Phys. Rev. C **49**, 2950 (1994).
[26] S. A. Coon, M. D. Scadron, P. C. McNamee, B. R. Barret, D. W. E. Blat, and B. H. J. McKellar, Nucl. Phys. **A317**, 242 (1979).
[27] S. A. Coon and W. Glöckle, Phys. Rev. C **23**, 1790 (1981).
[28] R. Machleidt, Adv. Nucl. Phys. **19**, 189 (1989).
[29] D. Plümper, J. Flender, and M. F. Gari, Phys. Rev. C **49**, 2370 (1994); J. A. Eden and M. F. Gari, *ibid.* **53**, 1510 (1996).
[30] A. Stadler, J. Adam, Jr., H. Henning, and P. U. Sauer, Phys. Rev. C **51**, 2896 (1995).
[31] E. O. Alt and M. Rauh, Few-Body Syst. **17**, 121 (1994).